

A readout-integrated time-bin qutrit analyzer for echo-based quantum memories

Adrian Holzäpfel,¹ Antonio Ortu,¹ and Mikael Afzelius¹

¹*Département de Physique Appliquée, Université de Genève, CH-1211 Genève, Switzerland*

(Dated: April 1, 2022)

We present a method to project time-bin qutrits stored in an echo-based quantum memory using several successive partial readouts of the memory. We demonstrate how this scheme can be used to implement projections onto a full set of mutually unbiased bases and, therefore, enables the characterization of arbitrary quantum states. Further, we study the integration of this protocol for the case of atomic frequency comb spin-wave storage by simulating the full storage process and performing a storage experiment with bright time-bin pulses in $^{151}\text{Eu}^{3+}:\text{Y}_2\text{SiO}_5$. In this context, a compound pulse for implementing partial readouts in quick succession is introduced and characterized.

I. INTRODUCTION

Long distance quantum networks would allow for a plethora of applications ranging from unconditionally secure communication to distributed quantum simulation and computation [1]. The prerequisite for long-distance links within such a network is the efficient mapping of information stored in photonic degrees of freedom to and from quantum memories [2–4]. A common proposal for such networks is to encode information in two dimensional degrees of freedom, such that each flying photon carries one quantum bit (qubit) of information. Encoding in higher dimensional spaces, however, has been shown to have several advantages over the encoding in qubits, showing a higher resilience to noise [5–7] as well as improved secret-key rates in quantum key distribution [8–10].

A suitable candidate for implementing high dimensional photonic quantum states are time-bin qudits. For these, entangled states can be readily generated [11, 12], and temporally multimode quantum memories can be used for their storage [13–16]. For time-bin qubits it has been demonstrated that in certain types of echo-based optical memories, projective measurements can be conveniently integrated into the readout process [17–19]. Specifically, two successive partial readouts can be used to interfere neighboring time-bins and, as such, allow for projection onto superposition states. This approach is equivalent to the use of an unbalanced Mach-Zehnder interferometer (uMZI) to perform time-bin qubit projections [19]. While such a Mach-Zehnder analyzer (MZA) can be readily generalized to higher dimensions by increasing the amount of spatial modes of the uMZI [20], it is not immediately obvious how to implement an equivalent action with partial readouts of a quantum memory. For a partial readout analyzer (PRA) the atomic transitions that play the role equivalent to spatial modes in the MZA is principally limited to two.

In this article we propose a time-bin qutrit analyzer based on a succession of amplitude and phase-optimized 2-mode-beam-splitter-like interactions. It is shown that such an analyser can exceed the conventional time-bin qutrit analyser based on 3-mode beam splitters in efficiency. The implementation of this protocol requires

several efficient partial readouts of the memory in close succession. To this end we propose a novel composite adiabatic pulse that can implement this action within the constraints of limited read/write power. A full qutrit storage and analysis scenario using the composite adiabatic pulses is simulated with Maxwell-Bloch simulations, based on the atomic frequency comb (AFC) spin-wave memory protocol. We also present an experimental AFC spin-wave implementation of the qutrit storage and analysis in a $^{151}\text{Eu}^{3+}:\text{Y}_2\text{SiO}_5$ crystal, in the regime of bright time-bin pulses.

II. THEORY

A time-bin qudit is formed by bringing a photon into a superposition of d possible arrival times, that we will represent as

$$|\psi\rangle = \sum_{i=0}^{d-1} a_i |i\rangle_t \quad (1)$$

where $|i+1\rangle_t$ denotes a temporally localized wave packet that is delayed by time-bin width τ from the otherwise identical wave packet $|i\rangle_t$. This time-bin qudit can be measured in the canonical basis $\{|i\rangle_t\}_{i=0}^{d-1}$ simply by performing time resolved single photon detection. But a full characterization of the quantum state requires measurements with a complete set of complementary observables. For a time-bin qubit ($d = 2$), for example, simple time resolved detection corresponds to a measurement of Pauli operator σ_z . For a full characterization we would like to also implement measurements of the Pauli operators σ_x and σ_y .

The MZA is a common method for implementing these measurements that relies solely on passive, linear optical components. It uses an uMZI to interfere neighboring time-bins, as illustrated in figure 2 (a). The uMZI consists of two arms of different length such that a photon taking the longer path through the device is delayed by τ relative to a photon taking the shorter path. Thus, the possibility of a photon arriving in the earlier time-bin but taking the long path through the device and a photon arriving late but taking the short path interfere

at the output. By adjusting the phase between the two paths of the uMZI appropriately, we can realize projections onto states of the form $\frac{1}{\sqrt{2}}(|0\rangle_t + e^{i\phi}|1\rangle_t)$ which in particular includes the eigenstates of σ_x and σ_y .

We note that this MZA is only conclusive in 50% of the cases, as an early photon might as well take the short path, or a late one the long path, in which case no interference will take place. This issue can be avoided by replacing the first beam splitter with an active switch [21]. The losses of currently available switches, however, relativize the advantage of having no inconclusive results, such that passive devices are commonly used. In the following we will compare our method only to the conventional MZA with passive components.

For on-demand and temporally multi-mode quantum memories like CRIB/GEM [22–24], ROSE [25, 26] or AFC spin-wave storage [27, 28], an equivalent action can be performed by means of two successive partial readouts of a stored time-bin qubit [19]. We consider a quantum memory consisting of a lambda system with a long-lived spin transition $|g\rangle - |s\rangle$ and two optical transitions, $|s\rangle - |e\rangle$ and $|g\rangle - |e\rangle$. The latter interacts as interface that absorbs flying photon. The resulting coherence in the optical transition is then mapped onto the spin transition by means of an optical π -pulse on $|s\rangle - |e\rangle$ (write pulse). For retrieval, the coherence is mapped back onto $|g\rangle - |e\rangle$ by another π -pulse (read pulse) and, subsequently, re-emitted as a flying photon based on a process that is dependent on the particular protocol in use. This storage sequence is sketched out in figure 1.

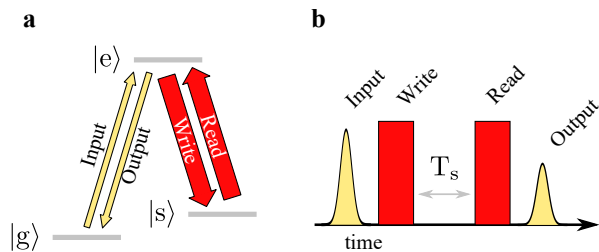


Figure 1. **Energy structure (a) and temporal sequence (b) of quantum storage in a lambda system.** The incoming photon (input) is absorbed on transition $|g\rangle - |e\rangle$. An optical π -pulse (write) is mapping the resulting coherence onto the long-lived transition $|g\rangle - |s\rangle$. After a storage time of T_s the coherence is mapped back onto $|g\rangle - |e\rangle$ by another optical π -pulse (read) and re-emitted as a flying photon (output). When considering the action of the read/write pulses, the memory can be treated as a two-level system with states $|s\rangle$ and $|e\rangle$, as $|g\rangle$ is unaffected by these pulses.

For implementing a partial readout analyzer (PRA) the π -pulse is replaced by two $\pi/2$ -pulses. If they are spaced apart by the width of one time-bin and the second partial readout occurs before the first emission of the memory, then their resulting action is completely equivalent to the MZA where $|s\rangle$ and $|e\rangle$ take on the role of the two spatial modes of the uMZI. This is illustrated in figure 2 (b). The PRA is particularly useful for measuring

time-bin qubits when the photons have a very long coherence time > 100 ns. The corresponding uMZI would require an optical path length difference of several meters or more between its two arms, such that stabilization becomes challenging. A quantum memory on the other hand is by its very nature capable of generating the required coherent delay.

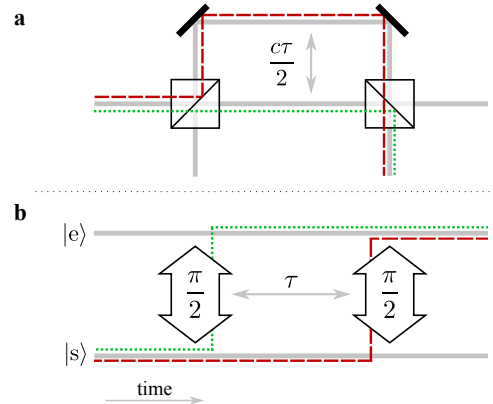


Figure 2. **Two equivalent methods for measuring superposition states of time-bin qubits.** (a) An uMZI with overall path difference $\Delta s = c\tau$ interferes adjacent time-bins with bin width τ . (b) An equivalent projector can be implemented by means of two partial readouts of a quantum memory. As the time evolution in the storage state $|s\rangle$ can be considered frozen, coherence that is mapped to the excited state via the green, dotted path will rephase τ earlier than coherence following the red, dashed path. The equivalent paths in the uMZI are indicated in the same color scheme.

The MZA can be readily generalized to three dimensions. If each 2-mode beamsplitter is replaced by a 3-mode beamsplitter (tritter), any photon passing through the uMZI may take three different paths of different optical path length, such that all time-bins of a qutrit can interfere with each other [20]. For the PRA, however, it is not immediately clear how to generalize the time-bin projection scheme to higher dimensions. As $|s\rangle$ and $|g\rangle$ are the equivalent to the spatial modes in the uMZI, the number of modes cannot be increased beyond two. We will demonstrate how despite this we can implement an efficient analyzer scheme.

Naively, one might expect that one can use three partial readouts of the memory to overlap three neighboring time-bins in complete analogy to the qubit PRA. However, while for the qubit case each generated delay inherits its phase from exactly one readout pulse, for the qutrit case two possible quantum paths through the interferometer lead to the same delay, as illustrated in figure 3. One of these paths inherits the phases from all readout pulses. As consequence the phase and amplitude of this delay depends non-trivially on the phase and amplitude of all of the readout pulses.

We will use an effective model of the partial readouts to put this into quantitative terms. For this purpose we will

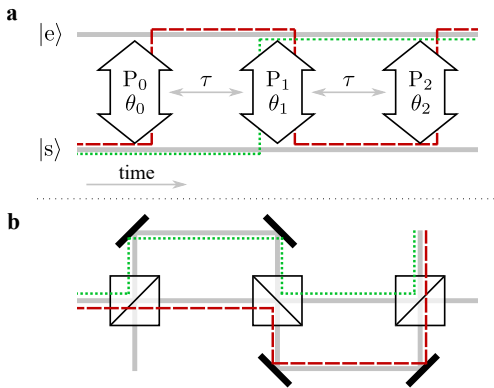


Figure 3. **Illustration of the readout-based qutrit analyzer.** (a) Each projection is implemented by applying three partial readouts with variable pulse area P_i and phase θ_i with a relative delay of τ between each. There are two interfering quantum paths resulting in a delay of τ that are indicated by the dashed red and dotted green line respectively. (b) This linear optics circuit is equivalent to the partial-readout scheme above. Once more the two interfering quantum paths are indicated.

describe the system as a tensor product $\mathbf{H}_t \otimes \mathbf{H}_s$, where \mathbf{H}_t represents the time-bin space as introduced in equation 1 and \mathbf{H}_s represents the internal state of the memory, which can be either $|s\rangle$ or $|e\rangle$ and specifies whether a given coherence is transition $|g\rangle \leftrightarrow |s\rangle$ or $|g\rangle \leftrightarrow |e\rangle$.

We choose this notation to highlight the equivalence between the PRA and a 2-mode linear optical device, where $|s\rangle$ and $|e\rangle$ would correspond to two spatial modes. It should be noted, however, that for the PRA strictly speaking \mathbf{H}_t describes coherences on either spin transition $|g\rangle \leftrightarrow |s\rangle$ or optical transition $|g\rangle \leftrightarrow |e\rangle$. The time-bin state that eventually will be emitted by the memory corresponds to whatever coherence has been mapped to $|g\rangle \leftrightarrow |e\rangle$ after all three partial readout pulses have been applied.

The effect of an ideal readout pulse with an arbitrary phase and area on the $|s\rangle$ - $|e\rangle$ transition can then be written as:

$$\mathbf{A} = \mathbf{Id}_t \otimes \begin{pmatrix} a & b \\ -b^* & a \end{pmatrix}_s \quad (2)$$

with

$$a = \sqrt{1 - P}$$

$$b = e^{i\theta} \sqrt{P}$$

where P is the transfer probability and θ the phase of the pulse.

Coherences on the spin transition can be considered frozen in their time evolution while coherences on the optical transition are experiencing rephasing. That means

that the rephasing of any coherence stored in the spin transition is delayed by one time-bin if the system is left to freely evolve for a time τ . We can model this evolution with the effective operator

$$\mathbf{B} = \mathbf{C}_t \otimes |s\rangle\langle s|_s + \mathbf{Id}_t \otimes |e\rangle\langle e|_s \quad (3)$$

with

$$\mathbf{C}_t = \sum_{i=0}^{\infty} |i+1\rangle \langle i|$$

Applying three readout pulses with free evolution of τ in-between them then performs the following unitary operation on the system.

$$\mathbf{U} = \mathbf{A}_2 \mathbf{B} \mathbf{A}_1 \mathbf{B} \mathbf{A}_0 \quad (4)$$

The element of this matrix that we are interested in is the one that maps from $|g\rangle \leftrightarrow |e\rangle$ to $|g\rangle \leftrightarrow |e\rangle$. We find the following expression

$$\begin{aligned} \langle e | \mathbf{U} | s \rangle = \\ -b_0^* a_1 a_2 \mathbf{Id}_t - a_0 b_1^* a_3 \mathbf{C}_t + b_0^* b_1 b_2^* \mathbf{C}_t - a_0 a_1 b_2^* \mathbf{C}_t^2 \end{aligned} \quad (5)$$

Ordering by experienced delay shows that a time-bin eigenstate entering the interferometer will exit as a superposition of three time-bins with complex amplitudes

$$\begin{aligned} \zeta_0 &= -a_0 a_1 b_2^* \\ \zeta_1 &= -a_0 b_1^* a_2 + b_0^* b_1 b_2^* \\ \zeta_2 &= -b_0^* a_1 a_2 \end{aligned} \quad (6)$$

To implement a given projection, it needs to be ensured that these three amplitudes have the appropriate magnitude and phase. Ideally, we would like to construct projections onto a complete set of mutually unbiased bases (MUBs) [29]. For a d -dimensional Hilbert space this is a set of $d + 1$ orthonormal bases

$$\mathcal{S}_{\text{MUB}} = \{ \{ |\psi_i^l\rangle \}_{i=0}^{d-1} \}_{l=0}^d \quad (7)$$

where the i indexes the states within a basis and m the different bases, such that the inner product of any two vectors from two different bases has the same magnitude

$$m \neq n : |\langle \psi_i^m | \psi_j^n \rangle|^2 = \frac{1}{d} \quad (8)$$

When such a set exists, it allows to fully characterize arbitrary states with the least amount of redundancy in-between measurements and can be seen as the higher dimensional generalization of characterizing a qubit by measuring with all three Pauli operators [30]. In three dimensions any vector of a basis that is mutually unbiased to the canonical one can be written in the form

$$|\psi\rangle = \frac{1}{\sqrt{3}} (e^{i\phi_0} |0\rangle_t + e^{i\phi_1} |1\rangle_t + e^{i\phi_2} |2\rangle_t) \quad (9)$$

Basis	ϕ_0	ϕ_1	ϕ_2	$P_{0,2}$	P_1	θ_0	θ_1	θ_2	η
MUB 1	0	0	0	$(3 - \sqrt{3})/6$	1/3	0	0	0	1/3
	0	$-2/3\pi$	$2/3\pi$	$(3 - \sqrt{3})/6$	1/3	$2/3\pi$	$-2/3\pi$	0	1/3
	0	$2/3\pi$	$-2/3\pi$	$(3 - \sqrt{3})/6$	1/3	$-2/3\pi$	$2/3\pi$	0	1/3
MUB 2	0	0	$-2/3\pi$	0.276	0.286	$-2/3\pi$	-0.388	0	0.429
	0	$-2/3\pi$	0	0.276	0.286	0	-2.482	0	0.429
	$-2/3\pi$	0	0	0.276	0.286	0	-0.388	$-2/3\pi$	0.429
MUB 3	0	0	$2/3\pi$	0.276	0.286	$2/3\pi$	0.388	0	0.429
	0	$2/3\pi$	0	0.276	0.286	0	2.482	0	0.429
	$2/3\pi$	0	0	0.276	0.286	0	0.388	$2/3\pi$	0.429
Optimal basis	0	$\pi/2$	0	0.5	0.2	0	$\pi/2$	0	3/5
	$-2/3\pi$	$\pi/2$	$2/3\pi$	0.5	0.2	$2/3\pi$	$\pi/2$	$-2/3\pi$	3/5
	$2/3\pi$	$\pi/2$	$-2/3\pi$	0.5	0.2	$-2/3\pi$	$\pi/2$	$2/3\pi$	3/5

Table I. **Pulse parameters and theoretically predicted efficiency for three MUBs and the optimal basis.** Each basis consists of three projectors of the form $(e^{i\phi_0} |0\rangle + e^{i\phi_1} |1\rangle + e^{i\phi_2} |2\rangle)/\sqrt{3}$. The three readout pulses to implement a given projector have the transfer probabilities P_i and the phases θ_i , the resulting projection an efficiency of η .

As it will be shown, projection onto this state with a PRA scheme can be achieved by implementing the following mapping

$$\begin{aligned} \mathbf{U}_\psi |n\rangle_t |s\rangle = & \\ & \sqrt{\frac{\eta}{3}} (e^{-i\phi_2} |n\rangle_t + e^{-i\phi_1} |n+1\rangle_t + e^{-i\phi_0} |n+2\rangle_t) |e\rangle \\ & + \sqrt{1-\eta} |\psi\rangle_t |s\rangle \end{aligned} \quad (10)$$

where $\eta \in [0, 1]$ and $|\psi\rangle_t$ symbolizes all coherence that has not been mapped onto $|g\rangle \leftrightarrow |e\rangle$ after all three pulses have been applied.

Once we have implemented this mapping, we can perform the desired projection by time resolved detection after the memory.

$$\begin{aligned} |\phi\rangle &= \alpha |0\rangle_t + \beta |1\rangle_t + \gamma |2\rangle_t; \\ |\langle e|_s \langle 2|_t \mathbf{U}_\psi |\phi\rangle |s\rangle|^2 &= \eta |\langle \psi|\phi\rangle|^2 \end{aligned} \quad (11)$$

In other words, after applying \mathbf{U}_ψ , the detection probability of a photon in time-bin $|2\rangle_t$ is proportional to the overlap of the stored state $|\phi\rangle$ and $|\psi\rangle$, the MUB state onto which we want to project the stored state. It reaches a maximum of η when the two states are identical. We will refer to η as the efficiency of the analyzer.

A step-by-step procedure on how to find the optimal choice for all parameters for a given projector is presented in detail in the appendix IV A. A summary of optimal parameters for a complete set of bases that are mutually unbiased to each other and the canonical basis (MUBs) is found in table I (upper half). We note that the efficiency of the projections is dependent on the exact choice of the phases. This is a consequence of the aforementioned interference of two quantum paths contributing to the same delay. In its presence the magnitude of this delay and its relative phase with regard to the other two delays are no longer independent.

Besides this set of observables, we have investigated one more measurement basis. Instead of deciding for a

specific projection and then finding the read pulse phases that implement it, we choose the phases such that they allow for fully constructive interference of the two quantum paths that result in the same delay. Then, the efficiency η of the resulting analyzer is maximal. Constructive interference will occur whenever $\phi_0 = -\phi_2$ and $\phi_1 = \pm\pi/2$. An example for a measurement basis that can be constructed from vectors of this form is appended to table I. The efficiency of this configuration is not only the optimal one for the proposed three-partial-readouts scenario, but indeed it can be shown that there can be no unitary black box that implements this action in a more efficient manner, as demonstrated in the appendix (IV C). We further note that its efficiency is considerably higher than the value of 1/3 that is reached for projections in the usual 3-mode analyzer scheme.

III. IMPLEMENTATION IN AN AFC SPIN-WAVE MEMORY

To confirm the experimental feasibility of our theoretical considerations, we have applied them to the case of atomic frequency comb (AFC) spin-wave storage. We have studied its performance both within the scope of a Maxwell-Bloch simulation of the storage and readout sequence, as well as in a storage experiment with bright time-bin pulses.

The implementation of an AFC spin-wave memory requires a lambda-system with a long-lived spin transition $|g\rangle - |s\rangle$ and an optical transition $|g\rangle - |e\rangle$. The optical transition has to be inhomogeneously broadened, with the inhomogeneous linewidth exceeding the homogeneous one by far. Then, an AFC can be prepared by frequency-selective optical pumping ions from $|g\rangle$ into an auxiliary state [31]. If a comb of periodicity Δ absorbs a train of pulses, the resulting coherence will rephase after a storage time of $T_{\text{AFC}} = 1/\Delta$ resulting in coherent re-emission. In order to allow for on-demand, long-duration storage, a write pulse on transition $|e\rangle - |s\rangle$ is applied

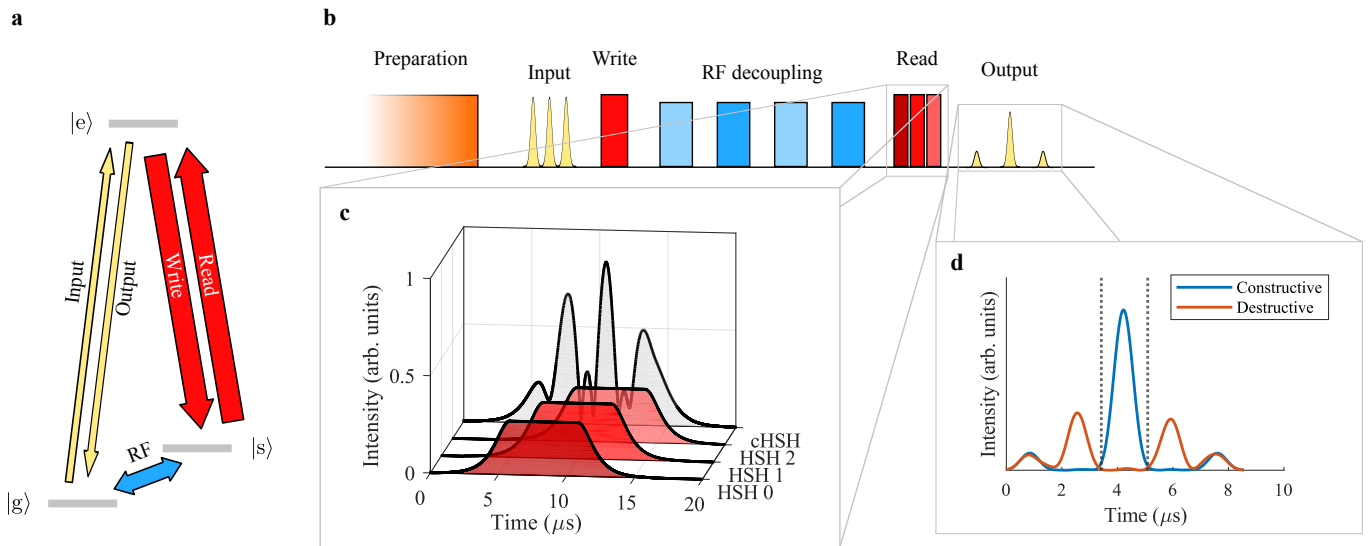


Figure 4. **AFC spin-wave storage with integrated PRA scheme.** (a) Level structure of the memory. (b) Temporal experimental sequence. (c) For the memory readout, we send a composite pulse that consists out of three overlapping HSH pulses (envelopes shown in red). An example for the envelope of the resulting composite HSH (cHSH) pulse is shown in gray. (d) Examples of simulated qutrit interference traces for constructive (blue) and destructive (red) interference. The interference bin is marked with dotted vertical lines.

before the rephasing has occurred. This pulse converts the optical coherence into a spin coherence on transition $|g\rangle - |s\rangle$. To preserve this coherence, several radio-frequency (RF) pulses may be applied to compensate for dephasing stemming from an inhomogeneous broadening of the spin transition and to dynamically decouple from the environment [32]. The stored light is retrieved by applying a readout pulse on $|e\rangle - |s\rangle$ to map the coherence back onto $|g\rangle - |e\rangle$. There, it will rephase due to the AFC and, finally, be re-emitted. This experimental sequence is illustrated in figure 4 (a) and (b).

For implementing the PRA scheme, the readout pulse is replaced with three partial readouts as described in section II. Here, a difficulty arises from experimental constraints. Efficient multimode AFC storage requires long optical lifetime and, therefore, typically is implemented in systems with low optical oscillator strength. This means that the optical Rabi frequency is often small in comparison to the bandwidth of the memory. Accordingly, efficient write/read pulses can only be implemented with an adiabatic profile. If the length of the resulting read pulse exceeds the width of the stored time-bins, then the partial readouts cannot be performed as a sequence of such adiabatic pulses. Deformation-less retrieval of the stored pulses, however, can only be ensured if rate and range of the frequency chirp of each read pulse are matched to those of the write pulse [33].

To perform two successive partial readouts despite these constraints we previously have proposed and implemented a composite pulse for analyzing time-bin qubits [16]. We extend this approach to the three partial readouts that are necessary to analyze qutrits and take the opportunity to have a closer look at its performance

in a Maxwell-Bloch simulation. The composite pulse is formed by overlapping several adiabatic pulses with a time delay of τ with respect to each other, such that the resulting electric field is given by the linear combination of the individual adiabatic profiles $f_{\text{adiab}}(t)$

$$E_{\text{comp}}(t) = \sum_{n=0}^2 E_i e^{i\theta_i} f_{\text{adiab}}(t + n\tau)$$

where θ_n can be set directly according to table I, while the field magnitude E_n has to be chosen such that the n -th partial readout has a total transfer probability of P_n as specified by the table. In this work we have combined three hyperbolic-square-hyperbolic (HSH) pulses [34] to form a composite HSH (cHSH) pulse, as illustrated in figure 4 (c). The HSH profile allows for a fast and uniform adiabatic transfer over a large bandwidth. It consists of a central region with constant Rabi frequency and chirp rate that is flanked by a smooth ramp up and ramp down of the field with a hyperbolic secant profile [35]. The pulse shape is fully characterized by its total chirp range Γ , duration of ramp up/ramp down T_H , duration of region with constant Rabi frequency T_S and the duration of the truncation window T_C to which the pulse is confined.

A. Maxwell-Bloch simulation

The storage process is simulated by numerically solving the semi-classical Maxwell-Bloch (MB) equations for two classical fields, the input/output mode and the write/read mode interacting with the lambda system of the memory. These fields are assumed to be spatially one-

dimensional, forward propagating, with a slowly varying envelope. The specific implementation of this 3-level MB simulator is described in Refs. [36, 37]. Our main interest lies in observing whether the predicted efficiencies for PRA analyzers can be reached when using cHSH pulses with realistic pulse parameters. To this end we made several simplifications, namely we neglected inhomogeneous broadening on the spin transition and we did not include any population decay or dephasing terms in the Bloch equations. After the application of the write pulse, any remaining optical coherences were set to zero to take into account that in actual experiments the spin storage time is typically much longer than the coherence time of the optical transitions. This also avoids interferences due to remaining optical coherences during the memory readout phase.

Before implementing the PRA projectors, we have simulated a regular storage experiment as a reference for efficiency. The memory input is a train of three Gaussian pulses that are spaced apart by $\tau = 1.67 \mu\text{s}$ and have a full width at half maximum (FWHM) in intensity of $\tau_{\text{in}} = \tau/2.38$ with a hard cutoff duration of τ [28]. The optical transition is shaped to an AFC with optical depth $d = 4$, bandwidth $\text{BW} = 4 \text{ MHz}$ and finesse $F = \pi / [\arctan(2\pi/d)]$ [38]. Finally, write and read operations are performed by applying an HSH pulse with $\Gamma/(2\pi) = 1.5 \text{ MHz}$, $T_S = 6 \mu\text{s}$, $T_H = T_S/2$ and truncation window $T_C = 12 \mu\text{s}$. The peak Rabi frequency was set to $\Omega/(2\pi) = 350 \text{ kHz}$. With these parameters the simulation yields a total AFC spin-wave efficiency of $\eta_0 = 30.3\%$. This efficiency is almost exclusively limited by the theoretical efficiency of the AFC for the given finite optical depth, which is 32.1% [31].

The PRA method requires precise setting of the phase and transfer probability of each component of the cHSH pulse. Therefore, we have simulated the storage efficiency with a readout of varying amplitude and directly recorded the relationship between amplitude and transfer probability. By inverting and interpolating the recorded relationship we can ensure that each partial readout has precisely the intended area given in table I. An example trace of the simulated memory output of the PRA can be seen in figure 4 (d).

To characterize measurements in the four bases from table I we take the following approach. For each basis $\{|\psi_i\rangle, i \in \{0, 1, 2\}\}$ we simulate storage and readout for all possible combinations of input $|\psi_i\rangle_{\text{inp}}$ and PRA projection $|\psi_j\rangle_{\text{ana}}$. Then we can determine the average fidelity of measurements in this basis, so the fidelity between the target state and the state that is actually projected onto

$$F = \frac{\sum_i |\text{ana} \langle \psi_i | \psi_i \rangle_{\text{inp}}|^2}{\sum_{ij} |\text{ana} \langle \psi_j | \psi_i \rangle_{\text{inp}}|^2} \quad (12)$$

We also record the average efficiency η of each basis as a percentage of η_0 . The results are listed in table II.

As seen there, the simulation shows fidelities that are close to unity and an excellent agreement between the-

Basis	η (predicted)	η (simulation)	F
MUB 1	1/3	33.7%	99.1%
MUB 2	42.9%	42.5%	98.5%
MUB 3	42.9%	42.9%	98.0%
Opt. basis	3/5	61.9%	97.7%

Table II. **Efficiency and fidelity of PRA qutrit projections as observed in the Maxwell-Bloch simulation.** For each basis we report the average fidelity of projections in this basis and with the efficiency of the simulated analyzer with the one calculated in section II.

oretically predicted and simulated projection efficiency. That the theoretical upper bounds for the analyzer efficiency can be fully saturated also confirms that partial readouts grouped together in a composite pulse can retain their original pulse area, without cross-talk affecting their performance.

B. Experimental implementation

Finally, we have implemented our method in an AFC spin-wave experiment where we have stored qutrits encoded onto bright time-bin pulses. As platform we have chosen a $^{151}\text{Eu}^{3+}:\text{Y}_2\text{SiO}_5$ crystal with a doping concentration of 1000 ppm. The Y_2SiO_5 forms a biaxial crystal with polarization eigenaxes D_1, D_2, b [39]. The crystal is cut to a cuboid along these axes, with all laser beams traveling along the b -axis with their polarization oriented in D_1 -direction such that absorption is maximized. Its temperature is kept at 4K using a closed-cycle helium cryostat. The relevant level structure is shown in figure 5 (a). It consists of a ground and excited state that are connected by an optical transition of approximately 580.04 nm. Due to the Eu ion's nuclear spin of 5/2, the quadrupolar interaction separates both the ground and the excited state into three doublets each, that are tens of MHz apart from each other. As the inhomogeneous linewidth of the optical transition is of the order of GHz, we need to apply a class-cleaning procedure [40, 41] before every experimental sequence to ensure that we can optically address individual transitions. After this, we can define our lambda system as indicated in figure 5 (a).

All optical fields are generated from a tunable external cavity diode laser at 1160 nm that is frequency locked onto a high-finesse cavity, amplified and finally frequency doubled [42]. The resulting 580 nm beam is distributed onto three acousto-optic-modulators that supply three spatial modes for crystal preparation, write/read and input, respectively. Manipulation of the spin transition $|g\rangle - |s\rangle$ is performed with a coil connected to a resonance circuit [43] that is driven by a 100 W RF-amplifier. This experimental setup is illustrated in figure 5 (b).

For the storage experiment, we prepare an AFC with a bandwidth of 3 MHz and an inverse periodicity of $1/\Delta = 25 \mu\text{s}$. Then, we send a train of three bright Gaussian pulses that form our qutrit with a time-bin width of

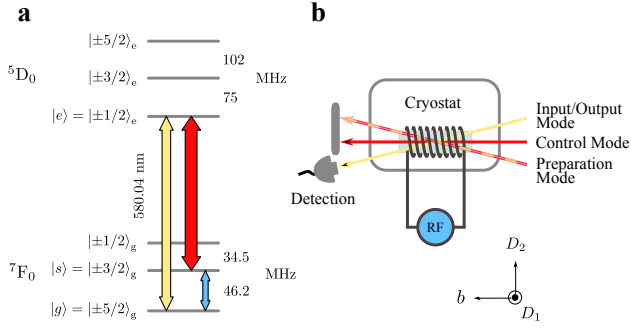


Figure 5. **Simplified schematics of the AFC spin-wave experiment in $^{151}\text{Eu}^{3+}:\text{Y}_2\text{SiO}_5$.** (a) Relevant atomic energy structure and transitions used in the memory protocol. (b) Simplified sketch of experimental setup

$\tau = 1.65 \mu\text{s}$. Each pulse is truncated to the time-bin width and has a FWHM of $\tau_{\text{in}}\tau/2.38$ [28]. To map the coherence onto the spin transition, we use an HSH write pulse with $\Gamma/(2\pi) = 1.5 \text{ MHz}$, $T_H = 1.65 \mu\text{s}$ and a square duration of $T_H = 7.5 \mu\text{s}$. The pulse is truncated to a window of $T_C = 15 \mu\text{s}$. For its peak Rabi frequency, we measure approximately 250 kHz. After being mapped to the spin transition, the coherence is stored there for 20 ms. To preserve coherence, we perform a single XY4 decoupling sequence [44]. Additionally, during the whole experiment we apply a static magnetic field of 1.35 mT along the D_1 -axis of the crystal which has been shown to increase the coherence time of the spin transition significantly [16, 45]. A more detailed description of this setup and a characterization of its performance as a memory platform can be found in Ref. [16].

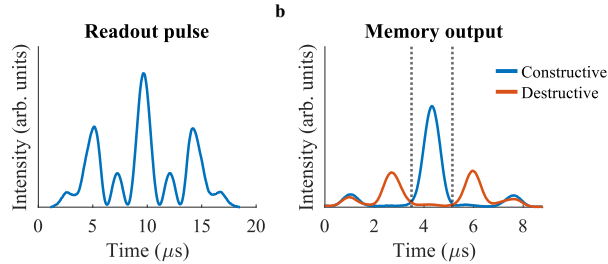


Figure 6. **Experimental traces** of readout (a) and memory output (b) as recorded by the photodetector.

For the retrieval of the coherence we finally apply a cHSH pulse that implements the desired PRA. The three partial readouts are identical to the write pulse, except for their phase and amplitude. While the phases can be set directly according to our calculations, the optimal amplitudes are found by manual optimization. Examples of a cHSH pulse and the resulting qutrit interference pattern at the output are shown in figure 6.

As before in the simulation, we have characterized the fidelity of the projectors by applying each of them to every vector of their respective basis. The resulting overlap matrices are shown in figure 7. The observed average fi-

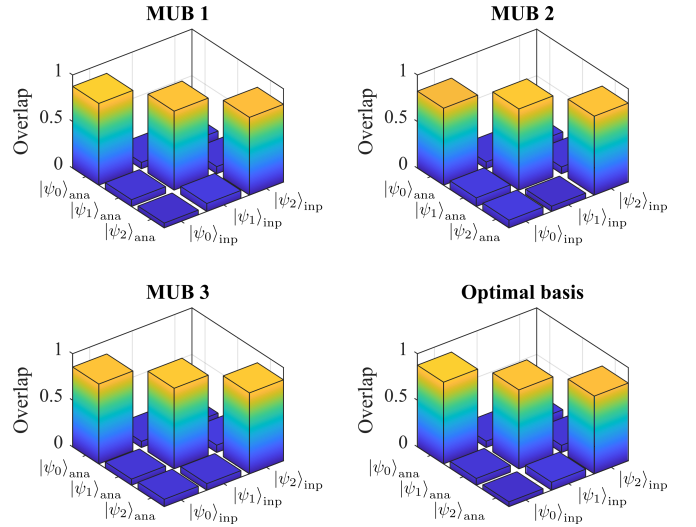


Figure 7. **Overlap matrices of the four investigated bases as measured in storage with bright time-bin pulses.** For each basis PRA projections of each combination of input and analyzer setting are performed and their overlap recorded. The diagonal elements correspond to the fidelity of the respective projection.

delity of the projectors is $F = (85 \pm 2)\%$. For sufficiently intense input pulses the spinwave storage is expected to essentially not affect the fidelity of the stored state because the noise generated by the storage process is negligible compared to the intensity of the retrieved light. Consequently, we can attribute any decrease in fidelity to imperfections of the qutrit measurement process. In order to determine whether the fidelity is limited by a unitary rotation of the analyzer from its nominal axis of projection, we have recorded visibility curves for one of the bases. For this purpose, we have measured the overlap for all three projectors while rotating the input state in two different sub-spaces. The resulting curves are shown in figure 8. For both sub-spaces we observe that the projector is rotated by approximately 10° from its nominal orientation. We estimate that the fidelity reported in the previous measurement could be increased by 3% if this unitary error was compensated.

IV. CONCLUSION

We have demonstrated how several partial readouts of a temporally multi-mode quantum memory can be used to project stored time-bin qutrits onto superposition states. The explicitly constructed projections onto a complete set of MUBs allow for the efficient characterization of arbitrary time-bin qutrit states. The Maxwell-Bloch simulation and storage experiment with bright pulses demonstrate that AFC spin-wave storage in conjunction with a compound pulse for the memory readout implement this measurement scheme in a way that can saturate the theoretically derived bound for projection

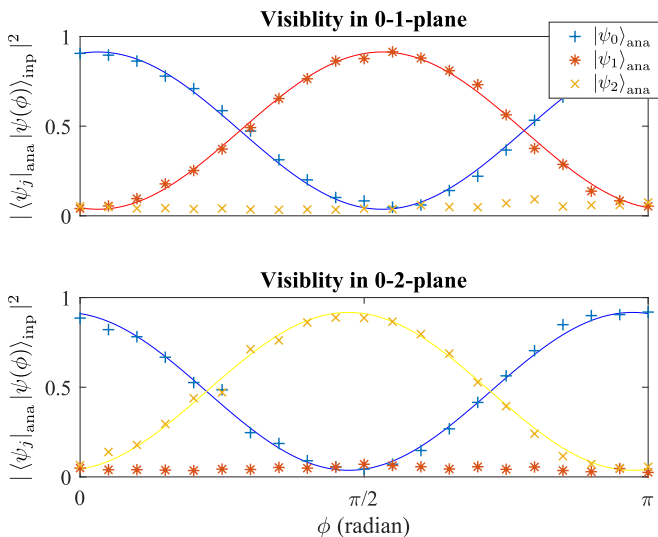


Figure 8. **Visibility measurement for the optimal basis in two different subspaces.** The overlap with with three basis states $|\psi\rangle_{\text{ana}}$ is recorded when the input is rotated in the 0-1-plane of the basis where

$|\psi(\phi)\rangle_{\text{inp}} = \cos \phi |\psi_0\rangle_{\text{inp}} + \sin \phi |\psi_1\rangle_{\text{inp}}$ and in the 0-2-plane where

$|\psi(\phi)\rangle_{\text{inp}} = \cos \phi |\psi_0\rangle_{\text{inp}} + \sin \phi |\psi_2\rangle_{\text{inp}}$.

The expectation value of the two projectors within the respective subspace is fitted with a sinusoidal model.

efficiency in an ideal scenario and enables precise state characterization even in presence of experimental imperfections.

The unitary operation that is implemented by the PRA scheme can also be realized as a linear optical device using only 2-mode beam splitters. This could be of interest since this device outperforms the 3-mode-splitter-based

approach to qutrit measurement in efficiency, though at the price of implementing just a single projection at a time instead of up to three simultaneously. This trade-off might be worthwhile when only a single projection is of interest or only a limited number of detection channels is available. In such a scenario, the efficiency could almost be doubled compared to usual 3-mode approach. An open question is how the presented approach generalizes to higher dimensions. For a d -dimensional system the efficiency of projections with a passive d -mode analyzer scales with $1/d$. In this regime the potential increase in efficiency from using a 2-mode analyzer might be even more substantial.

DATA AVAILABILITY

The data sets generated and/or analysed during the current study are available from the corresponding authors upon reasonable request.

ACKNOWLEDGEMENTS

We acknowledge funding from the Swiss FNS NCCR programme Quantum Science Technology (QSIT), European Union Horizon 2020 research and innovation program within the Flagship on Quantum Technologies through GA 820445 (QIA) and under the Marie Skłodowska-Curie program through GA 675662 (QCALL).

We also thank Nicolas Brunner and Sébastien Designolle from the Université de Genève for fruitful discussions and Jean Etesse from the Institut de Physique de Nice for his contributions to the experimental setup. Further, we thank Philippe Goldner and Alban Ferrier from Chimie ParisTech for fruitful discussions and for providing the crystals.

-
- [1] H. J. Kimble, The quantum internet, *Nature* **453**, 1023 (2008).
- [2] H.-J. Briegel, W. Dür, J. I. Cirac, and P. Zoller, Quantum repeaters: The role of imperfect local operations in quantum communication, *Phys. Rev. Lett.* **81**, 5932 (1998).
- [3] L.-M. Duan, M. D. Lukin, J. I. Cirac, and P. Zoller, Long-distance quantum communication with atomic ensembles and linear optics, *Nature* **414**, 413 (2001).
- [4] N. Sangouard, C. Simon, H. de Riedmatten, and N. Gisin, Quantum repeaters based on atomic ensembles and linear optics, *Rev. Mod. Phys.* **83**, 33 (2011).
- [5] D. Kaszlikowski, P. Gnaniński, M. Żukowski, W. Miklaszewski, and A. Zeilinger, Violations of local realism by two entangled N -dimensional systems are stronger than for two qubits, *Phys. Rev. Lett.* **85**, 4418 (2000).
- [6] T. Vértesi, S. Pironio, and N. Brunner, Closing the detection loophole in bell experiments using qudits, *Phys. Rev. Lett.* **104**, 060401 (2010).
- [7] S. Ecker, F. Bouchard, L. Bulla, F. Brandt, O. Kohout, F. Steinlechner, R. Fickler, M. Malik, Y. Guryanova, R. Ursin, and M. Huber, Overcoming noise in entanglement distribution, *Phys. Rev. X* **9**, 041042 (2019).
- [8] J. Mower, Z. Zhang, P. Desjardins, C. Lee, J. H. Shapiro, and D. Englund, High-dimensional quantum key distribution using dispersive optics, *Phys. Rev. A* **87**, 062322 (2013).
- [9] A. Acín, N. Brunner, N. Gisin, S. Massar, S. Pironio, and V. Scarani, Device-independent security of quantum cryptography against collective attacks, *Phys. Rev. Lett.* **98**, 230501 (2007).
- [10] L. Sheridan and V. Scarani, Security proof for quantum key distribution using qudit systems, *Phys. Rev. A* **82**, 030301 (2010).
- [11] H. De Riedmatten, I. Marcikic, H. Zbinden, and N. Gisin, Creating high dimensional time-bin entanglement using mode-locked lasers, arXiv preprint quant-ph/0204165 (2002).
- [12] H. de Riedmatten, I. Marcikic, V. Scarani, W. Tittel, H. Zbinden, and N. Gisin, Tailoring photonic entangle-

- ment in high-dimensional hilbert spaces, *Phys. Rev. A* **69**, 050304 (2004).
- [13] M. Gündoğan, P. M. Ledingham, K. Kutluer, M. Mazzera, and H. de Riedmatten, Solid state spin-wave quantum memory for time-bin qubits, *Phys. Rev. Lett.* **114**, 230501 (2015).
- [14] A. Tiranov, P. C. Strassmann, J. Lavoie, N. Brunner, M. Huber, V. B. Verma, S. W. Nam, R. P. Mirin, A. E. Lita, F. Marsili, M. Afzelius, F. Bussi eres, and N. Gisin, Temporal multimode storage of entangled photon pairs, *Physical Review Letters* **117**, 240506 (2016).
- [15] A. Tiranov, S. Designolle, E. Z. Cruzeiro, J. Lavoie, N. Brunner, M. Afzelius, M. Huber, and N. Gisin, Quantification of multidimensional entanglement stored in a crystal, *Phys. Rev. A* **96**, 040303 (2017).
- [16] A. Ortu, A. Holz apfel, J. Etesse, and M. Afzelius, Storage of photonic time-bin qubits for up to 20 ms in a rare-earth doped crystal (2021), [arXiv:2109.06669](https://arxiv.org/abs/2109.06669) [quant-ph].
- [17] N. Timoney, I. Usmani, P. Jobez, M. Afzelius, and N. Gisin, Single-photon-level optical storage in a solid-state spin-wave memory, *Phys. Rev. A* **88**, 022324 (2013).
- [18] M. U. Staudt, S. R. Hastings-Simon, M. Nilsson, M. Afzelius, V. Scarani, R. Ricken, H. Suche, W. Sohler, W. Tittel, and N. Gisin, Fidelity of an optical memory based on stimulated photon echoes, *Phys. Rev. Lett.* **98**, 113601 (2007).
- [19] M. Gündoğan, M. Mazzera, P. M. Ledingham, M. Cristiani, and H. de Riedmatten, Coherent storage of temporally multimode light using a spin-wave atomic frequency comb memory, *New Journal of Physics* **15**, 045012 (2013).
- [20] R. T. Thew, A. Acin, H. Zbinden, and N. Gisin, Bell-type test of energy-time entangled qutrits, *Physical review letters* **93**, 010503 (2004).
- [21] H. Bechmann-Pasquinucci and W. Tittel, Quantum cryptography using larger alphabets, *Phys. Rev. A* **61**, 062308 (2000).
- [22] A. Alexander, J. Longdell, M. Sellars, and N. Manson, Coherent information storage with photon echoes produced by switching electric fields, *Proceedings of the Ninth International Meeting on Hole Burning, Single Molecule, and Related Spectroscopies: Science and Applications, Hole Burning, Single Molecule, and Related Spectroscopies: Science and Applications*, *Journal of Luminescence* **127**, 94 (2007).
- [23] G. H etet, M. Hosseini, B. M. Sparkes, D. Oblak, P. K. Lam, and B. C. Buchler, Photon echoes generated by reversing magnetic field gradients in a rubidium vapor, *Opt. Lett.* **33**, 2323 (2008).
- [24] M. Sabooni, M. Jafarbeklu, and F. Sarreshtehdari, Broadband and efficient quantum memory using ac stark gradient echo memory, [arXiv preprint arXiv:2003.12821](https://arxiv.org/abs/2003.12821) (2020).
- [25] V. Damon, M. Bonarota, A. Louchet-Chauvet, T. Chaneli ere, and J.-L. L. Gou et, Revival of silenced echo and quantum memory for light, *New Journal of Physics* **13**, 093031 (2011).
- [26] M. Bonarota, J. Dajczgewand, A. Louchet-Chauvet, J.-L. L. Gou ot, and T. Chaneli ere, Photon echo with a few photons in two-level atoms, *Laser Physics* **24**, 094003 (2014).
- [27] A. Ortu, J. V. Rakonjac, A. Holz apfel, A. Seri, S. Grandi, M. Mazzera, H. de Riedmatten, and M. Afzelius, Multimode capacity of atomic-frequency comb quantum memories, [arXiv preprint arXiv:2202.12383](https://arxiv.org/abs/2202.12383) (2022).
- [28] A. Ortu, J. Rakonjac, A. Holz apfel, A. Seri, S. Grandi, H. de Riedmatten, and M. Afzelius, Multimode capacity of atomic-frequency comb quantum memories [unpublished manuscript] (2022).
- [29] H. Bechmann-Pasquinucci and A. Peres, Quantum cryptography with 3-state systems, *Phys. Rev. Lett.* **85**, 3313 (2000).
- [30] S. N. Filippov and V. I. Man'ko, Mutually unbiased bases: tomography of spin states and the star-product scheme, *Physica Scripta* **T143**, 014010 (2011).
- [31] M. Afzelius, C. Simon, H. de Riedmatten, and N. Gisin, Multimode quantum memory based on atomic frequency combs, *Phys. Rev. A* **79**, 052329 (2009).
- [32] A. Holz apfel, J. Etesse, K. T. Kaczmarek, A. Tiranov, N. Gisin, and M. Afzelius, Optical storage for 0.53 s in a solid-state atomic frequency comb memory using dynamical decoupling, *New Journal of Physics* **22**, 063009 (2020).
- [33] J. Min ar, N. Sangouard, M. Afzelius, H. de Riedmatten, and N. Gisin, Spin-wave storage using chirped control fields in atomic frequency comb-based quantum memory, *Phys. Rev. A* **82**, 042309 (2010).
- [34] M. Tian, T. Chang, K. D. Merkel, and W. Randall, Reconfiguration of spectral absorption features using a frequency-chirped laser pulse, *Appl. Opt.* **50**, 6548 (2011).
- [35] F. de S eze, F. Dahes, V. Crozatier, I. Lorger e, F. Bretnaker, and J.-L. Le Gou et, Coherent driving of tm^{3+} : yag ions using a complex hyperbolic secant optical field, *The European Physical Journal D - Atomic, Molecular, Optical and Plasma Physics* **33**, 343 (2005).
- [36] J. Minar, *Coherent control, quantum memories and quantum repeaters*, *Ph.D. thesis* (2010), iD: unige:39728.
- [37] M. Afzelius, I. Usmani, A. Amari, B. Lauritzen, A. Walther, C. Simon, N. Sangouard, J. Min ar, H. de Riedmatten, N. Gisin, and S. Kr oll, Demonstration of atomic frequency comb memory for light with spin-wave storage, *Phys. Rev. Lett.* **104**, 040503 (2010).
- [38] M. Bonarota, J. Ruggiero, J. L. L. Gou et, and T. Chaneli ere, Efficiency optimization for atomic frequency comb storage, *Phys. Rev. A* **81**, 033803 (2010).
- [39] C. Li, C. Wyon, and R. Moncorge, Spectroscopic properties and fluorescence dynamics of er^{3+} and yb^{3+} in $\text{y}_2\text{si}_2\text{o}_7$, *IEEE Journal of Quantum Electronics* **28**, 1209 (1992).
- [40] P. Jobez, N. Timoney, C. Laplane, J. Etesse, A. Ferrier, P. Goldner, N. Gisin, and M. Afzelius, Towards highly multimode optical quantum memory for quantum repeaters, *Phys. Rev. A* **93**, 032327 (2016).
- [41] B. Lauritzen, N. Timoney, N. Gisin, M. Afzelius, H. de Riedmatten, Y. Sun, R. M. Macfarlane, and R. L. Cone, Spectroscopic investigations of Eu^{3+} : Y_2SiO_5 for quantum memory applications, *Phys. Rev. B* **85**, 115111 (2012).
- [42] P. Jobez, I. Usmani, N. Timoney, C. Laplane, N. Gisin, and M. Afzelius, Cavity-enhanced storage in an optical spin-wave memory, *New Journal of Physics* **16**, 083005 (2014).
- [43] A. Ortu, *Rare earth quantum memories: spectroscopy of a new platform and quantum storage implementations*, Ph.D. thesis, University of Geneva (2022).
- [44] T. Gullion, D. B. Baker, and M. S. Conradi, New, compensated carr-purcell sequences, *Journal of Magnetic Resonance* (1969) **89**, 479 (1990).
- [45] J. Etesse, A. Holz apfel, A. Ortu, and M. Afzelius, Optical

and spin manipulation of non-kramers rare-earth ions in a weak magnetic field for quantum memory applications, *Physical Review A* **103**, 022618 (2021).

APPENDIX

A. Finding the parameters for the implementation of PRA

As explained in section II, the implementation of the PRA for projecting onto state $\frac{1}{\sqrt{3}}(e^{i\phi_0}|0\rangle + e^{i\phi_1}|1\rangle + e^{i\phi_2}|2\rangle)$ requires to find the optimal pulse parameters for three partial readouts such that they perform the mapping

$$\begin{aligned} \mathbf{U}|n\rangle_t|s\rangle = & \\ & \sqrt{\frac{\eta}{3}}(e^{-i\phi_2}|n\rangle_t + e^{-i\phi_1}|n+1\rangle_t + e^{-i\phi_0}|n+2\rangle_t)|e\rangle \\ & + \sqrt{1-\eta}(\dots)|s\rangle \end{aligned} \quad (13)$$

with the highest possible efficiency η . A particularly interesting set of projections are the following three bases that are mutually unbiased to each other and the canonical basis (MUBs).

$$\begin{aligned} \text{MUB1} \quad & \frac{1}{\sqrt{3}}(|0\rangle + |1\rangle + |2\rangle) \\ & \frac{1}{\sqrt{3}}(|0\rangle + e^{-i2/3\pi}|1\rangle + e^{i2/3\pi}|2\rangle) \\ & \frac{1}{\sqrt{3}}(|0\rangle + e^{i2/3\pi}|1\rangle + e^{-i2/3\pi}|2\rangle) \\ \text{MUB2} \quad & \frac{1}{\sqrt{3}}(|0\rangle + |1\rangle + e^{-i2/3\pi}|2\rangle) \\ & \frac{1}{\sqrt{3}}(|0\rangle + e^{-i2/3\pi}|1\rangle + |2\rangle) \\ & \frac{1}{\sqrt{3}}(e^{-i2/3\pi}|0\rangle + |1\rangle + |2\rangle) \\ \text{MUB3} \quad & \frac{1}{\sqrt{3}}(|0\rangle + |1\rangle + e^{i2/3\pi}|2\rangle) \\ & \frac{1}{\sqrt{3}}(|0\rangle + e^{i2/3\pi}|1\rangle + |2\rangle) \\ & \frac{1}{\sqrt{3}}(e^{i2/3\pi}|0\rangle + |1\rangle + |2\rangle) \end{aligned} \quad (14)$$

We have derived that a time-bin eigenstate entering the readout-based analyzer is mapped onto a superposition with complex amplitudes

$$\begin{aligned} \zeta_0 &= -a_0a_1b_2^* \\ \zeta_1 &= -a_0b_1^*a_2 + b_0^*b_1b_2^* \\ \zeta_2 &= -b_0^*a_1a_2 \end{aligned} \quad (15)$$

with $a_i = \sqrt{1-P_i}$ and $b_i = e^{i\theta_i}\sqrt{P_i}$. For our convenience we factor out a global phase of π as such a phase does

not affect the state on which we project and yield

$$\begin{aligned}
z_0 &= a_0 a_1 b_2^* \\
&= \sqrt{(1-P_0)(1-P_1)P_2} e^{-i\theta_2} \\
z_1 &= a_0 b_1^* a_2 - b_0^* b_1 b_2^* \\
&= \sqrt{(1-P_0)P_1(1-P_2)} e^{-i\theta_1} \\
&\quad - \sqrt{P_0 P_1 P_2} e^{i(-\theta_0 + \theta_1 - \theta_2)} \\
z_2 &= b_0^* a_1 a_2 \\
&= \sqrt{P_0(1-P_1)(1-P_2)} e^{-i\theta_0}
\end{aligned} \tag{16}$$

The first and last bin inherit their phase directly from the first and last partial readout pulse, such that we can immediately conclude that we should set

$$\begin{aligned}
\theta_0 &= \phi_2 \\
\theta_2 &= \phi_0
\end{aligned} \tag{17}$$

Further we demand that the signals in both these bins have the same magnitude.

$$\begin{aligned}
|z_0|^2 &= |z_2|^2 \\
\implies (1-P_0)(1-P_1)P_2 &= P_0(1-P_1)(1-P_2) \\
\implies P_0 &= P_2
\end{aligned} \tag{18}$$

This leaves P_0, P_1 and θ_1 as free parameters. Both the magnitude as well as the phase of the central bin depend on all three of these parameters. We define

$$\begin{aligned}
\tilde{z}(P_0, \theta_1) &= z_1 / \sqrt{P_1} \\
&= \sqrt{1-P_0} \sqrt{1-P_2} e^{-i\theta_1} - \sqrt{P_0} \sqrt{P_2} e^{i(\theta_1 - \theta_0 - \theta_2)} \\
&= (1-P_0) e^{-i\theta_1} - P_0 e^{i(\theta_1 - \phi_0 - \phi_2)}
\end{aligned}$$

(19)

In order to implement the respective desired projector, we need to ensure that the central bin has the proper phase.

$$\phi_1 = -\arg(\tilde{z}) \tag{20}$$

and the same amplitude as the outer bins

$$|z_1|^2 = P_1 |\tilde{z}|^2 \stackrel{!}{=} |z_0|^2 = |z_2|^2 \tag{21}$$

Before we move to the individual MUBs, we note that there exist certain classes of analyzers that share the same efficiency η . For demonstrating this, we first use the global phase freedom to set

$$\begin{aligned}
\tilde{\phi}_0 &= \phi_0 - \phi_1 \\
\tilde{\phi}_1 &= \phi_1 - \phi_1 = 0 \\
\tilde{\phi}_2 &= \phi_2 - \phi_1
\end{aligned} \tag{22}$$

which is possible without loss of generality. Then, equation 19 and, consequently, equation 20 and 21 are only

dependent on the P_i and the sum $\tilde{\phi}_{\text{tot}} = \tilde{\phi}_0 + \tilde{\phi}_2$. From this follows that all projectors with the same $\tilde{\phi}_{\text{tot}}$ share the same optimal choice for $\theta_1 = \tilde{\theta}_1$, the same optimal transfer probabilities P_i and the same efficiency η . Once the initial global phase rotation is undone, this leads to the optimal phase settings

$$\begin{aligned}
\theta_0 &= \phi_2 \\
\theta_2 &= \phi_0 \\
\theta_1 &= (\tilde{\theta}_1 + \phi_1)
\end{aligned} \tag{23}$$

We will refer to measurements that are related like this to being of the same efficiency class. It should be noted that all projectors of any given MUB from equation 14 belong to the same efficiency class. That means that in the following we can determine the optimal $\tilde{\theta}_1$ and P_i for just a single projector from each basis and then determine the optimal parameters for the other two by making use of equation 23.

1. MUB 1

We consider the projection on the first projector of MUB 1. As we set $\theta_0 = \theta_2 = 0$ in accordance to equation 17, equation 20 now becomes

$$0 = \arg(\tilde{z}) = \arg((1-P_0)e^{i\theta_1} - P_0e^{-i\theta_1}) \tag{24}$$

For $P_0 > 0.5$ the equation is solved by $\theta_1 = \pi$, and $\theta_1 = 0$ for $P_0 < 0.5$. In both cases the magnitude is $|\tilde{z}| = |1 - 2P_0|$. Now we demand that the central and outer bins are of equal magnitude (eq. 21) and find

$$(1 - 2P_0)^2 P_1 = (1 - P_0) P_1 (1 - P_0) \tag{25}$$

This expression is only linear in P_1 . We can solve for $P_1(P_0)$ and express the magnitude of the time-bins, and therefore η , purely in terms of P_0 .

$$\eta = 3 \cdot (1 - 2P_0)^2 P_1(P_0) \tag{26}$$

We maximize it so that the resulting analyzer has the highest possible efficiency and conclude

$$\begin{aligned}
P_0 &= (3 - \sqrt{3})/6 \approx 0.21 \\
P_1 &= 1/3 \\
\tilde{\theta}_1 &= 0
\end{aligned} \tag{27}$$

2. MUB 2 and 3/general case

For MUB 2 and 3 we follow a similar route as for MUB 1. Unlike for the latter, no analytical solution has been found. The final optimization step is performed numerically. The approach shown in the following will work for finding PRAs that implement projections onto arbitrary states of the form $\frac{1}{\sqrt{3}} (e^{i\phi_0} |0\rangle + e^{i\phi_1} |1\rangle + e^{i\phi_2} |2\rangle)$ after

transforming them according to equation 22.

We once more demand that the phase of the central bin is zero.

$$\begin{aligned} \phi_2 = 0 &\stackrel{!}{=} \arg(\tilde{z}) \\ \implies \\ 0 = \text{Im}(\tilde{z}) &= (1 - P_0) \sin(\theta_1) + P_0 \sin(\theta_1 - \phi_0 - \phi_2) \\ &= (1 - P_0) \sin(\theta_1) + P_0 \sin(\theta_1 - \phi_{\text{tot}}) \end{aligned} \quad (28)$$

Solving for θ_1 gives

$$\theta_1(P_0) = \text{acot} \left(\frac{1/P_0 - 1 + \cos(\phi_{\text{tot}})}{\sin(\phi_{\text{tot}})} \right) \quad (29)$$

We insert $\theta_1(P_0)$ into equation 21 and solve for $P_1(P_0)$. Once more we have all ingredients for expressing the total efficiency as a function of P_0 .

$$\eta = 3 \cdot (1 - 2P_0)^2 P_1(P_0) \quad (30)$$

We can determine the maximum numerically and find

$$\begin{aligned} \tilde{\theta}_1 &= -0.388 \\ P_0 &= 0.2764 \\ P_1 &= 0.2857 \\ \eta &= 0.4286 \end{aligned} \quad (31)$$

and

$$\begin{aligned} \tilde{\theta}_1 &= 0.388 \\ P_0 &= 0.2764 \\ P_1 &= 0.2857 \\ \eta &= 0.4286 \end{aligned} \quad (32)$$

respectively.

B. Optimal basis

In order to achieve the highest possible efficiency for the given scheme we have to maximize the magnitude of \tilde{z} from equation 19. This will be the case whenever

$$e^{-i\theta_1} = -e^{i(\theta_1 - \phi_0 - \phi_2)} \quad (33)$$

One possible choice is

$$\begin{aligned} \phi_0 &= -\phi_2 \\ \theta_1 &= \pi/2 \end{aligned} \quad (34)$$

The equal bin amplitude condition equation 21 then simply reads:

$$P_1 = (1 - P_0)P_0(1 - P_1) \quad (35)$$

As for the previous bases we solve for $P_1(P_0)$ and subsequently maximize $\eta(P_0)$. We find that the optimal parameter choice and resulting efficiency then reads

$$\begin{aligned} \tilde{\theta}_1 &= \pi/2 \\ P_0 &= 0.5 \\ P_1 &= 0.2 \\ \eta &= 3/5 \end{aligned} \quad (36)$$

Finally, we can find two more orthogonal vectors of the same efficiency class and arrive at the basis

$$\begin{aligned} &|0\rangle + i|1\rangle + |2\rangle \\ \text{MUB1} \quad &e^{-i2/3\pi} |0\rangle + i|1\rangle + e^{i2/3\pi} |2\rangle \\ &e^{i2/3\pi} |0\rangle + i|1\rangle + e^{-i2/3\pi} |2\rangle \end{aligned} \quad (37)$$

C. Optimal unitary black box

Generally speaking, our device implements the qutrit projections by mapping several time-bins onto one and thereby interfering them. Clearly, such a device cannot be 100% efficient, as it would turn orthogonal inputs into collinear ones, and therefore not be unitary. We can ask what limit on its efficiency we can derive from the unitarity of the device alone. For this purpose, we consider a unitary black box that performs the following mapping.

$$\begin{aligned} \mathbf{U} |n\rangle_t |0\rangle_s &= \sqrt{\frac{\eta}{3}} (|n\rangle_t + e^{i\phi_1} |n+1\rangle_t + e^{i\phi_2} |n+2\rangle_t) |0\rangle_s \\ &\quad + \sqrt{1-\eta} |\psi_n\rangle \end{aligned} \quad (38)$$

$|\psi_n\rangle$ is a unit length vector that contains any contribution that is ending up in the dark port. We can conclude the following.

$$\begin{aligned} 0 &= |\langle 0_s, 2_t | 0_t, 0_s \rangle| \\ &= |\langle 0_s, 2_t | \mathbf{U}^\dagger \mathbf{U} | 0_t, 0_s \rangle| \\ &= (\sqrt{1-\eta} \langle \psi_2 | + \sqrt{\frac{\eta}{3}} \langle 0 |_s (\langle 2 |_t + e^{-i\phi_1} \langle 3 |_t + e^{-i\phi_2} \langle 4 |_t)) \\ &\quad * (\sqrt{\frac{\eta}{3}} (|0\rangle_t + e^{i\phi_1} |1\rangle_t + e^{i\phi_2} |2\rangle_t) |0\rangle_s + \sqrt{1-\eta} |\psi_0\rangle) \\ &= |\frac{\eta}{3} e^{i\phi_2} + (1-\eta) \langle \psi_2 | \psi_0 \rangle| \\ \iff & \frac{\eta}{3} e^{i(\phi_2 - \phi_0)} = -(1-\eta) \langle \psi_2 | \psi_0 \rangle \\ \implies & \frac{\eta}{3} = (1-\eta) |\langle \psi_2 | \psi_0 \rangle| \end{aligned} \quad (39)$$

A bound that we can immediately derive from this is the following

$$\begin{aligned} \frac{\eta}{3} &= (1 - \eta) |\langle \psi_2 | \psi_0 \rangle| \\ &\leq (1 - \eta) \\ \implies \\ \eta &\leq \frac{3}{4} \end{aligned} \quad (40)$$

But we can derive an even tighter bound by taking the time translation symmetry of our interferometric device into account. Since any delay that the device applies is relative to the time of arrival of the input, the output into the dark ports can be expressed in the following general form.

$$|\psi_n\rangle = \sum_i a_i |n+i\rangle_t |1\rangle_s \quad (41)$$

1. Three consecutive non-zero time bins in the dark port

Before we look at the case of arbitrarily many temporal modes, let us consider the simple case of a device that distributes onto three temporal modes. In this case we can continue from the result of equation 39 as follows.

$$\begin{aligned} \frac{\eta}{3} &= (1 - \eta) |\langle \psi_2 | \psi_0 \rangle| \\ &= (1 - \eta) |\langle 1|_s (a_2^* \langle 4|_t + a_1^* \langle 3|_t + a_0^* \langle 2|_t) \\ &\quad (a_0 |0\rangle_t + a_1 |1\rangle_t + a_2 |2\rangle_t) |s\rangle| \\ &= (1 - \eta) |a_0| |a_2| \\ &\leq (1 - \eta) |a_0| \sqrt{1 - |a_0|^2} \\ &\leq \frac{1 - \eta}{2} \\ \implies \\ \eta &\leq \frac{3}{5} \end{aligned} \quad (42)$$

In the fourth line we make use of the fact that $|\psi_n\rangle$ are normalized vectors and in the fifth line we bound $|a_0| \sqrt{1 - |a_0|^2}$ from above by its maximum of $\frac{1}{2}$.

2. Arbitrarily many non-zero time bins in the dark port

We will see that allowing for arbitrary many modes does not affect this argument. We can show that if we map onto three temporal modes in the bright port, only up to three consecutive temporal modes in the dark port can be populated.

Assuming that there is a finite amount of temporal modes, there exist a k such that for each input $|n\rangle_t |0\rangle_s$

a_{n+k} is the first non-zero component of the vector $|\psi_n\rangle$, so

$$\begin{aligned} a_{n+k} &\neq 0 \\ \forall i < n+k : a_i &= 0 \end{aligned} \quad (43)$$

Further, as there are only finitely many non-zero coefficients, there must be an l , such that every coefficient after a_{n+k+l} is guaranteed to be zero.

$$\forall i > n+k+l : a_i = 0 \quad (44)$$

For any inputs $|n+l\rangle_t |0\rangle_s$, $|n\rangle_t |0\rangle_s$ with $l > 2$ there is no overlap in the bright port. Their overlap in the dark port must therefore also be zero. In this scenario, when calculating this overlap we find

$$\begin{aligned} 0 &= \langle \psi_n | \psi_{n+l} \rangle \\ &= \left(\sum_i a_i^* \langle 1|_s \langle n+i|_t \right) \left(\sum_j a_j |n+l+j\rangle_t |1\rangle_s \right) \\ &= \sum_i \sum_j a_i^* a_j \delta_{n+i, n+l+j} \\ &= \sum_i a_{i+n+l}^* a_{i+n} \\ &= a_{n+k+l}^* a_{n+k} \end{aligned} \quad (45)$$

$\delta_{n+i, n+l+j}$ in line 3 is a Kronecker delta. From the second to last line we use that for any other term either one or the other coefficient is zero because of condition 43 or condition 44, respectively.

As a_{n+k} is per assumption non-zero, a_{n+k+l} must be zero. Therefore we can now state that only coefficients from a_{n+k} to $a_{n+k+(l-1)}$ can be non-zero. As we reduced the range of possibly non-zero components by one, we can now apply the same proof for the case of $|\psi_n\rangle$ and $|\psi_{n+l-1}\rangle$ and will conclude that $a_{n+k+l-1} = 0$. We can apply the proof iteratively and reduce the range of possibly non-zero components one by one, right until we reach the case of $|\psi_n\rangle$ and $|\psi_{n+2}\rangle$ where the overlap in the bright port will no longer be zero. Such that we can finally conclude

$$\forall l > 2 : a_{n+k+l} = 0 \quad (46)$$

This means there can always be only three consecutive non-zero time bins in the dark port. Even allowing for arbitrarily many time-bins in the dark port, the problem will ultimately be equivalent to the one treated in section IV C 1.